

Expansive Open Fermi Arcs and Connectivity Changes Induced by Infrared Phonons in ZrTe_5

Lin-Lin Wang

Ames Laboratory, U.S. Department of Energy, Ames, IA 50011, USA

(December 3, 2020)

Abstract

Expansive open Fermi arcs covering most of the surface Brillouin zone (SBZ) are desirable for detection and control of many topological phenomena, but so far has been only reported for Kramers-Weyl points, or unconventional chiral fermions, pinned at time-reversal invariant momentum in chiral materials. Here using first-principles band structure calculations, we show that for conventional Weyl points in ZrTe_5 with the chirality of $+1/-1$ near the BZ center at general momentum induced by one of the infrared phonons, the second lowest B_{1u} mode for breaking inversion symmetry, they can also form expansive open Fermi arcs across the SBZ boundary to occupy most of the SBZ when projected on (001) surface. We reveal that such expansive open Fermi arcs are evolved from the topological surface states that connect multiple surface Dirac points on the (001) surface of the topological insulator phases without lattice distortion in ZrTe_5 . Furthermore, we find that the connectivity of the induced open Fermi arcs can be changed by the magnitude of the lattice distortion of this infrared phonon mode. Thus, we propose that using coherent optical phonon to modulate lattice parameters can offer ways to induce novel topological features including expansive open Fermi arcs and dynamically control Fermi arcs connectivity in ZrTe_5 .

llw@ameslab.gov

I. Introduction

Weyl fermions¹ can emerge in systems where time-reversal symmetry (TRS) or inversion symmetry (IS) or both are broken. Weyl points (WPs) of opposite chirality in momentum space are monopoles (sinks or sources) for Berry² curvature. The projection of WPs on a surface without overlap are connected via open-ended Fermi arcs. Weyl fermions give rise to novel topological properties, such as chiral anomaly³⁻⁵, chiral magnetoelectric effect^{6, 7}, anomalous Hall effect⁸, circular photo-galvanic effect⁹⁻¹², Weyl orbits¹³⁻¹⁵ and nonlocal transport¹⁶. The WPs at general momentum of Brillouin zone (BZ) formed from two-band crossing with the chirality of +1/-1 are conventional WPs and appear in pairs. Recent studies¹⁷⁻²⁰ have extended the chiral fermions to unconventional cases or Kramers-Weyl points that are pinned at time-reversal invariant momentum (TRIM) with high degeneracy and chirality in chiral materials, such as RhSi and CoSi. The corresponding open Fermi arcs are expansive and can cover the whole surface Brillouin zone (SBZ). In contrast, because conventional WPs are split from either Dirac points by breaking TRS^{21, 22} or the same band inversion by breaking IS²³, the distance among conventional WPs and the corresponding open Fermi arcs are usually small compared to the size of SBZ.

However, here we show that for the conventional WPs emerging near the Γ point in ZrTe₅ induced by one of the infrared (IR) phonon, the second lowest B_{1u} mode, to break IS and transform the strong or weak topological insulator (TI) phase into a Weyl semimetal (WSM), the open Fermi arcs can also be expansive on ZrTe₅ (001) surface to cross BZ boundary and span most of the SBZ. We further reveal that such expansive behavior arises from the topological surface states connecting the multiple surface Dirac points (SDPs) on (001) for the TI phases of ZrTe₅ without lattice distortion. This shows that surface terminations of a TI with multiple SDPs²⁴ can be used as the platform to induce expansive open Fermi arcs, in addition to Kramers-Weyl in chiral materials¹⁷⁻²⁰. Expansive open Fermi arcs have the advantage for easy detection and versatile manipulation to realize many topological phenomena, such as spin texture, Weyl orbits¹³⁻¹⁵ and nonlocal transport¹⁶. The connectivity of open Fermi arcs from WP projections, either within the SBZ (intra-SBZ) or crossing the SBZ boundary (inter-SBZ), depends on the detailed surface band structures²⁵. Here we show that the connectivity of open Fermi arcs on ZrTe₅ (001) surface can be dynamically controlled by the magnitude of the lattice distortion of

this B_{1u} phonon mode. On the same surface termination of ZrTe_5 (001), this B_{1u} mode can drive the open Fermi arcs connectivity from intra-SBZ to inter-SBZ.

ZrTe_5 has attracted intensive interest because it is near the phase boundary between a strong TI (STI) and a weak TI (WTI). A single layer of ZrTe_5 has been predicted²⁶ to be a quantum spin Hall insulator, while the 3D ZrTe_5 crystal is either a STI or WTI depending on the small changes in structural parameters used in the band structure calculations. The reason for such behavior is from the band inversion between p orbitals of two different Te sites at Γ point, which is very sensitive to the small change in atomic positions. Different experiments have also provided a range of evidence indicating the scenarios from Dirac semimetal (DSM)²⁷ to TIs²⁸ to WSM²⁹. A recent study³⁰ has shown that the different properties can be due to different concentration of defects from different growth methods. In high magnetic field, the WPs induced by breaking TRS have also been proposed to explain the anomalous Hall conductivity²⁹. Such sensitive dependence of topological states on the small structural change in ZrTe_5 offers the opportunity for controlling topological phase transitions³¹. Temperature³², pressure, volume³³ and strain³⁴ have been shown to drive the WTI-STI transition with a critical DSM in between for ZrTe_5 . Thus, lattice distortion from optical phonon modes can be used very effectively to induce topological phase transition in ZrTe_5 , such as WSM, which has been proposed in other systems²³ where IS is removed by IR phonon modes. Recently in a Terahertz (THz) optical pump-probe experiment, we have induced the STI-DSM-WTI topological phase transition in ZrTe_5 by a coherent Raman phonon³⁵ mode for retaining the IS.

In this paper, we first report the calculated phonons for ZrTe_5 from density functional theory^{36, 37} (DFT) and compare the zone-center modes to experimental data. Next, we show that the IR phonon, namely two lowest B_{1u} modes, can induce two pairs of WPs around Γ point near the Fermi energy (E_F) by breaking IS. More importantly, for the second lowest B_{1u} mode, these induced conventional WPs with large enough lattice distortion can change Fermi arcs connectivity and have expansive open Fermi arcs when projected on (001) surface. Then we reveal that such expansive open Fermi arcs arise from the topological surface states connecting the multiple surface Dirac points (SDPs) on (001) for the TIs without lattice distortion. Thus, we propose that surface terminations with multiple SDPs connected by topological surface states can be used as platforms to induce expansive open Fermi arcs and dynamically change Fermi arcs connectivity by coherent optical phonon to modulate lattice parameters.

II. Computational Methods

Phonons of ZrTe_5 have been calculated with density functional perturbative theory³⁸ (DFPT) using PBE³⁹ exchange-correlation (XC) functional with D2 parameters⁴⁰ for van der Waals (vdW) interaction in DFT^{36, 37} as implemented in Quantum Espresso⁴¹ (QE). We use a Γ -centered Monkhorst-Pack⁴² ($9 \times 9 \times 5$) k -point mesh for the primitive ZrTe_5 base-centered orthorhombic cell of 12 atoms. For the electronic band structure calculations, the atomic displacements from the chosen optical phonon mode are applied to the experimental lattice parameters⁴³ to study the phonon induced topological phase transitions. Spin-orbit coupling (SOC) effect is included in all band structure calculations, which are performed in Vienna Ab initio Simulation Package^{44, 45} (VASP) with a plane-wave basis set and projector augmented wave (PAW) method⁴⁶. The kinetic energy cutoff is 816 eV for norm-conserving pseudo-potentials in QE and 230 eV for PAW in VASP. The convergence with respect to k -point mesh has been carefully checked, with total energy converged below 1 meV/cell. For ionic relaxation, the absolute magnitude of force on each atom is reduced below 0.005 eV/Å. The relaxation in VASP is with an increased kinetic energy cutoff of 287 eV. For phonon calculations, the small displacement method in VASP and Phonopy⁴⁷ have also been used. A ($3 \times 3 \times 2$) q-point mesh is used with the primitive unit cell for DFPT calculation and a ($4 \times 2 \times 2$) supercell of 384 atoms built with the conventional unit cell is used for the small displacement method. To calculate topological properties, a tight-binding (TB) model based on maximally localized Wannier functions (MLWFs)^{48, 49} has been constructed to reproduce closely the band structure including SOC in the range of $E_F \pm 1\text{eV}$. Then the spectral functions and Fermi surface (FS) of a semi-infinite surface are calculated using the surface Green's function methods⁵⁰⁻⁵³ as implemented in WannierTools⁵⁴.

III. Results and Discussion

A. Crystal structure and phonons

The crystal structure of ZrTe_5 (Fig.1(a)) has a base-centered orthorhombic unit cell in space group 63 ($Cmcm$). It has a layered structure along b -axis with Zr and apical Te (Te_a)

occupying the $4c$ site, while dimer Te (Te_d) and zigzag Te (Te_z) occupying the $8f$ site. The base center is on the ab plane. The crystal structure can also be seen as a particular arrangement of ZrTe_8 clusters, which includes Zr and the neighboring Te atoms (two Te_a , four Te_d and two Te_z). Along a -axis, the cluster by itself is quite close-packed. Then along c -axis, the oppositely aligned clusters form sheets in sharing a zig-zag Te chain at the boundaries. Lastly, the ZrTe_5 sheets are loosely stacked along b -axis with vdW interaction. So the natural cleaving plane gives (010) surface. The next easy to cleave is (001) surface breaking among the zig-zag Te_z chain. These two surfaces and the corresponding 2D SBZs in relation to the bulk BZ are shown in Fig.1(b). The crystal structure has two mirror planes, one normal to the a -axis and other to c -axis, and also a glide plane normal to the b -axis.

The calculated phonon band structure and density of states (DOS) are plotted in Fig.1(c) and (d), respectively. There are two types of phonons showing small or large band dispersion. The phonons with small band dispersion correspond to intra-cluster modes and have sharp peaks in DOS, mostly in the higher energy range beyond 70 cm^{-1} . The phonons with large band dispersion correspond to mostly relative motions of the ZrTe_8 clusters and have broad peaks in DOS below 70 cm^{-1} . The two inversion centers of the crystal structure are not inside ZrTe_8 clusters, but with one being between the clusters and the other at the mid-point of Te_z - Te_z bond, as shown by the black circles in Fig.1(e) and (f). This means some of the low-energy IR modes can be effective in breaking the IS. Additional phonon calculations using the small displacement method and also PBEsol⁵⁵, a different XC functional, are shown in the Appendix to give good agreement.

With the PBE³⁹ XC functional and also D2 parameters⁴⁰ for vdW interaction, the dimensions of the relaxed unit cell are $a=3.985 \text{ \AA}$, $b=14.393 \text{ \AA}$ and $c=13.629 \text{ \AA}$, which agree very well to the experimental data⁴³ (within 1%) of $a=3.987 \text{ \AA}$, $b=14.502 \text{ \AA}$ and $c=13.727 \text{ \AA}$. The low-energy zone-center phonon modes are listed in Table 1. The PBE-D2 XC functional gives better agreement with experimental data⁵⁶ than local density approximation^{57, 58} (LDA), which over-binds, gives smaller lattice parameters for the fully relaxed unit cells and overestimates the phonon frequencies in most cases. Among the listed optical phonon modes, the A_{1g} Raman mode of 37.6 cm^{-1} is the one that we have studied to induce WTI-DSM-STI topological phase transition³⁵. To study the effect of breaking IS on topological band structure to induce WPs, we choose the two lowest B_{1u} IR mode of 25.7 and 44.1 cm^{-1} at zone center. The first lowest B_{1u}

mode as depicted in Fig.1(e) mostly involves the torsional movement of the ZrTe_8 clusters around the a -axis. The second lowest B_{1u} mode mostly involves the atomic displacements of Te_a toward zig-zag Te_z chain along c -axis as shown in Fig.1(f). We introduce the parameter of λ to describe the magnitude of the lattice distortion. For the first lowest B_{1u} mode of 25.7 cm^{-1} with $\lambda=1.0$, it corresponds to the lattice distortion of 0.005 \AA for Zr, 0.025 \AA for Te_a , 0.030 \AA for Te_d and 0.035 \AA for Te_z , respectively. For the second lowest B_{1u} mode of 44.1 cm^{-1} with $\lambda=1.0$, it involves the lattice distortion of 0.014 \AA for Zr, 0.056 \AA for Te_a , 0.015 \AA for Te_d and 0.025 \AA for Te_z , respectively. Notably for the second lowest B_{1u} mode, there is a large displacement of Te_a along the c -axis in perpendicular to the (001) surface, which can induce a much larger change in the topological surface states than the first lowest B_{1u} mode. In the following, we will focus on this second lowest B_{1u} mode that induces expansive open Fermi arcs on (001) surface and then also discuss the first lowest B_{1u} mode for comparison.

B. Bulk band structures and induced Weyl points

The electronic band structures of ZrTe_5 with the second lowest B_{1u} lattice distortion are presented in Fig.2. For reference, the band structure of ZrTe_5 without lattice distortion is plotted in Fig.2(a). The small flat piece along Γ - Y in Fig.2(a) is the band inversion between Te_d and Te_z p orbitals with a small gap of 30 meV giving a STI phase with the topological index⁵⁹ of (1;110). With broken IS induced by the second B_{1u} mode (44.1 cm^{-1}) lattice distortion ($\lambda=1.0$) in Fig.2(b), the band double degeneracy along most high-symmetry directions are lifted. Especially along Γ - Y direction, the top valence and bottom conduction band move closer toward each other and still maintain the band inversion as zoomed in Fig.2(c). This indicates WPs arising from the crossings between valence and conduction bands are nearby and slightly off the high-symmetry direction. After searching over the whole BZ with the MLWF-based TB model, we found two pairs of WPs near the Γ point.

Although the lattice distortion is along the c -axis, the two pairs of WPs emerge on the k_x - k_y plane at $k_z=0$. The Berry curvature has been calculated for one of two pairs of WPs along k_x in Fig.2(d) and confirms these band crossings are indeed WPs with chirality or Chern number $C=+/-1$, i.e., source and sink of Berry curvature. Their energy-momentum coordinates are $(E_F; \pm 0.002, \pm 0.076, 0.000 \text{ \AA}^{-1})$. The other pair of WPs is related to this pair by the mirror or 2-fold rotation. The distance among WPs along k_y is much larger than that along k_x . With increasing

magnitude of the B_{1u} mode lattice distortion, as shown in Fig.2(e) and (f) for $\lambda=1.5$ and 2.0, respectively, the band gap along Γ - Y direction increases while maintaining the same band inversion features. The location of the band inversion along the Γ - Y direction changes very little. the increasing size of the gap means the location of the WPs must move mostly in the k_x direction. Indeed, we find the energy-momentum coordinates of the two pairs of WPs are moved to $(E_F+4\text{meV}; \pm 0.010, \pm 0.089, 0.000 \text{ \AA}^{-1})$ and $(E_F+9\text{meV}; \pm 0.014, \pm 0.104, 0.000 \text{ \AA}^{-1})$ for $\lambda=1.5$ and 2.0, respectively.

C. (001) surface: expansive open Fermi arcs and connectivity changes

One unique behavior of WPs is the open Fermi arcs connecting the WP projections of opposite chirality on surfaces if there is no overlap. For ZrTe_5 , this surface is (001), where all four WPs have their own projections (see Fig.1(b)). As shown in Fig.3(a) for (001) top surface for the second lowest B_{1u} lattice distortion with $\lambda=1.0$, the projections of WPs form open Fermi arcs along k_y , while the distance along k_x is much smaller. The (001) bottom surface (Fig.3(b)) have the same termination as the (001) top surface, but becomes non-equivalent because of the B_{1u} mode breaking the IS. The open Fermi arcs on (001) bottom with $\lambda=1.0$ is more extensive than that on (001) top surface. When the magnitude of lattice distortion increases from $\lambda=1.0$ to 1.5, the distances among WPs increase mostly along k_x . As the WPs are pushed away from each other, the Fermi arcs are extended accordingly (Fig.3(c) and (d)). Notably, the open Fermi arcs also move closer to the other surface states. The open Fermi arcs are near the Γ point and the connectivity of the Fermi arcs so far is still within the first SBZ or intra-SBZ.

However, when the magnitude of the B_{1u} lattice distortion increase further to $\lambda=2.0$, we find that the open Fermi arcs connectivity changes from intra-SBZ to inter-SBZ. To clearly show the open Fermi arcs connectivity with respect to the (001) SBZ, the 2D Fermi surface (FS) for $\lambda=2.0$ at $E_F+9 \text{ meV}$ of the top surface is plotted with a zoom-out view in Fig.4(a). Strikingly although these WPs are still at general momentum near Γ point, unlike the open Fermi arcs for smaller λ or in other IS-broken WSMs, they extend beyond the first SBZ, cross the SBZ boundary and connect to those WP projections in the second SBZ along k_y . Such expansive open Fermi arcs on ZrTe_5 (001) surface is unique, as most open Fermi arcs connecting conventional WPs are small and intra-SBZ. Only open Fermi arcs connecting the highly degenerated Kramers-Weyl pinned at TRIM in chiral materials have such expansive range. On ZrTe_5 (001) bottom

surface in Fig.4(g), the open Fermi arcs is expansive too, but it does not cross the SBZ boundary at $\lambda=2.0$.

To reveal the reason for such expansive open Fermi arcs in the induced ZrTe₅ WSM, we use the STI phase of the undistorted lattice as reference and inspect the topological surface states. For the STI phase of ZrTe₅, unlike the easy cleaving (010) with only a single SDP at $\bar{\Gamma}$, (001) (Fig.4(b)) is known to have SDPs protected by TRS at three out of four TRIM points at $\bar{\Gamma}$, \bar{S} and \bar{S}' . The last TRIM point at \bar{Y} has a sizable band gap. The SDP at $\bar{\Gamma}$ is right at E_F , while the other two SDPs at \bar{S} and \bar{S}' have much lower energy at $E_F-0.55$ eV. Importantly these three SDPs are connected by the topological surface states expansive in the SBZ as seen in Fig.4(b). The topological surface states have large energy dispersion along most directions in the SBZ, except for $\bar{S}-\bar{S}'$, which is along k_y or b -axis. This is understandable because k_y direction is along the loosely vdW stacking direction. Such expansive surface states with similar band dispersion behavior also exist between bulk band N and $N-2$, almost parallel in energy-momentum profile at slightly lower energy. For the 2D FS of STI in Fig.4(e) at E_F+9 meV, there is clearly a SDP at $\bar{\Gamma}$. Then there is a small hole pocket along $\bar{\Gamma}-\bar{X}$ direction. The other SDPs are shown by the topological surface states running mostly along k_y direction and connecting to the neighboring SBZ. The surface states almost stay as straight lines along k_y , except around the $\bar{\Gamma}$ point with a bump.

With the second lowest B_{1u} lattice distortion of $\lambda=2.0$ to remove IS, the SDP at $\bar{\Gamma}$ point is gapped out as shown in Fig.4(c) and (d) for the top and bottom surface, respectively. For the top surface, the SDP at $\bar{\Gamma}$ point breaks off from bulk conduction band and moves to lower energy. The surface bands along other directions also move to lower energy and become just surface valence states, except that the band along $\bar{S}-\bar{Y}$ still connects with bulk conduction band. As the result, for 2D FS in Fig.4(f), the SDP at $\bar{\Gamma}$ disappear and the nearby hole pockets shrinks for shifting to lower energy, while two pairs of WP projections emerge. Most noticeable, the surface states running along k_y with a bump at $\bar{\Gamma}$ are now deformed to connect these four WP projections and become the expansive open Fermi arcs. In contrast for the bottom surface in Fig.4(d), the SDP at $\bar{\Gamma}$ breaks off from the bulk valence band and move to higher energy. The surface band along other directions also move to higher energy and become almost all surface conduction bands, again with the exception along the $\bar{S}-\bar{Y}$ direction for the one surface band still connecting

to bulk valence band. Because the surface states move to higher energy, the change in 2D FS for bottom surface in Fig.4(g) is quite large. As the SDP at $\bar{\Gamma}$ disappear, the two small hole pockets enlarge into open Fermi arcs connecting the four WP projections, but they do not cross the SBZ boundary yet, unlike those on the (001) top surface. The surface states running along k_y with bumps are pushed further away from $\bar{\Gamma}$ and become straight lines along k_y .

Thus, the topological surface states do not disappear upon topological phase transition to WSM, but deform into expansive open Fermi arcs. The spin texture in Fig.4(i) and (j) shows spin-momentum locking along the open Fermi arcs. Expansive open Fermi arcs have only been observed so far for Kramers-Weyl points pinned at TRIM in chiral crystals¹⁷⁻²⁰, such as RhSi and CoSi. For the two pairs of conventional WPs of $C=\pm 1$ at general momentum here in ZrTe₅ induced by the second lowest B_{1u} mode of 44.1 cm^{-1} , we predict expansive open Fermi arcs on the ZrTe₅ (001) surface. Note such expansive open Fermi arcs are topologically non-trivial features and also robust as shown in the Appendix for using PBEsol, a different XC functional in the DFT calculations. Extra calculations with the second lowest B_{1u} lattice distortion imposed on both the theoretically optimized (a STI) and slightly volume-expanded (a WTI) structural parameters also give similar expansive open Fermi arcs for ZrTe₅, because the topological surface states are similarly expansive on (001) in these two phases, with the STI having three while the WTI having two SDPs²⁶.

Additionally, in Fig.5(a), we show the crossover of the open Fermi arcs with the topological surface states at $\lambda=1.8$ for the second lowest B_{1u} lattice distortion that changes the Fermi arcs connectivity from intra-SBZ to inter-SBZ on the (001) top surface. The energy-momentum coordinates are $(E_F+7\text{meV}; \pm 0.013, \pm 0.098, 0.000 \text{ \AA}^{-1})$. When λ increases further to 3.0, the open Fermi arcs connectivity on the (001) top surface remain inter-SBZ and expansive with increasing distance among the WPs (Fig.5(c)) for the energy-momentum coordinates of $(E_F+15\text{meV}; \pm 0.019, \pm 0.135, 0.000 \text{ \AA}^{-1})$. Now the Fermi arcs connectivity on the (001) bottom surface also changes from intra-SBZ (Fig.5(b)) to inter-SBZ (Fig.5(d)). Thus, not only this second lowest B_{1u} mode in ZrTe₅ can be used to induce WPs, but also the magnitude of lattice distortion can be used to change the connectivity of the open Fermi arcs. We propose that coherent phonon of the second lowest B_{1u} mode of 44.1 cm^{-1} in optical pump-probe experiment can be used to dynamically change the surface Fermi arcs connectivity on ZrTe₅ (001) surface.

In a distinct contrast, for the first lowest B_{1u} mode of 25.7 cm^{-1} in ZrTe_5 , the induced open Fermi arcs on (001) surface are not expansive as shown in Fig.6. With the first B_{1u} lattice distortion increases from $\lambda=2.0$ (Fig.6(a) and (b)) to 6.0 (Fig.6(c) and (d)), the WPs separation increases along k_x , but the surface states have only small changes compared to the cases for the second lowest B_{1u} lattice distortion. The connectivity of the open Fermi arcs induced by the first B_{1u} mode does not change and remains only inside the first SBZ. The spectral functions in Fig.6(e) and (f) show also the much smaller change than those in Fig.4(c) and (d), which reflects in the much smaller energy shift of the SDPs at \bar{S} and \bar{S}' points. Notably for the second lowest B_{1u} mode (Fig.1(f)), there is a large displacement of Te_a along the c -axis in perpendicular to the (001) surface, which can induce a much larger change in (001) topological surface states than the first lowest B_{1u} mode (Fig.1(e)). Thus, topological surface states connecting multiple SDPs provide the stage for expansive open Fermi arcs, but the lattice distortion to break the IS still needs to be sufficiently large enough to deform the surface states.

D. (010) surface: surface states

Lastly, on ZrTe_5 (010) surface, in contrast to (001) surface, there are no expansive surface states for both STI and WSM in Fig.7(a) and (b), respectively. As zoomed in around $\bar{\Gamma}$ point, for STI in Fig.7(c), there is a single SDP at $\bar{\Gamma}$ protected by TRS inside the bulk band gap. With the second lowest B_{1u} lattice distortion of $\lambda=2.0$, there are two pairs of WPs induced on the $k_z=0$ plane. While the SDP is gapped out, the bulk band structure becomes gapless, as shown in Fig.7(d) by the touching point between bulk valence and conduction band projections along $\bar{\Gamma}-\bar{U}$. There is a short segment of surface state along $\bar{\Gamma}-\bar{U}$ coming out from the projections of the two pairs of WPs. As for the 2D FS on (010) surface at $E_F+9 \text{ meV}$ in the STI (Fig.7(e)), there is a circle arising from the surface Dirac cone around the $\bar{\Gamma}$ point. With the WSM induced by the B_{1u} lattice distortion (Fig.7(f)), the circle from the surface Dirac cone disappear. Although there are no open Fermi arcs because WPs of opposite chirality are projected onto each other, there are surface states at WP projections, just not open Fermi arcs.

As a final note, although the IS is broken by these B_{1u} modes, the induced two pairs of WPs are at the same energy because of the remaining mirror symmetry. Further symmetry-breaking is needed to separate the WPs to different energies to realize the recently proposed quantized circular photo-galvanic effect¹¹.

IV. Conclusion

In conclusion, we have shown that low-frequency infrared phonon modes in ZrTe_5 can be used to induce Weyl points by breaking inversion symmetry while still maintaining band inversion near Γ point. The two pairs of Weyl points induced by the second lowest B_{1u} mode beyond certain lattice distortion are connected by expansive open Fermi arcs crossing into neighboring surface Brillouin zones. Our study indicates that expansive open Fermi arcs are not unique to unconventional chiral fermions or Kramers-Weyl points pinned at time-reversal invariant momentum in chiral materials, but can also exist for conventional Weyl points with chirality of ± 1 at general momentum. The key for such expansive open Fermi arcs is the transformation of the topological surface states connecting the multiple surface Dirac points on (001) surface of ZrTe_5 upon topological phase transition. Furthermore, we find that the connectivity of the open Fermi arcs can be changed with different magnitude of the second lowest B_{1u} lattice distortion. Thus, we propose that topological surface states connecting multiple surface Dirac points with large enough lattice distortion from infrared phonon modes are platforms to induce expansive open Fermi arcs. Our study also shows the potential of using coherent optical control and ultrafast spectroscopy to induce and detect novel topological features including expansive open Fermi arcs and dynamically control of Fermi arcs connectivity in ZrTe_5 .

Acknowledgements

We acknowledge helpful discussion with Jigang Wang. This work was supported by the Center for the Advancement of Topological Semimetals, an Energy Frontier Research Center funded by U.S. Department of Energy (DOE), Office of Science, Basic Energy Sciences. Work was performed at Ames Laboratory, which is operated by Iowa State University under contract DE-AC02-07CH11358.

Mode (cm^{-1})	LDA	PBE-D2	Expt
B_{1g}	39.2	36.7	28
A_{1g}	43.4	37.6	39
B_{3g}	48.7	41.8	48
B_{3g}	80.1	79.4	62
B_{2g}	82.8	72.7	72
B_{2g}	99.0	96.3	88
B_{1u}	20.0	25.7	
B_{1u}	62.0	44.1	

Table 1. Zone-center optical phonon modes calculated in LDA and PBE-D2 in comparison to experimental data⁵⁶.

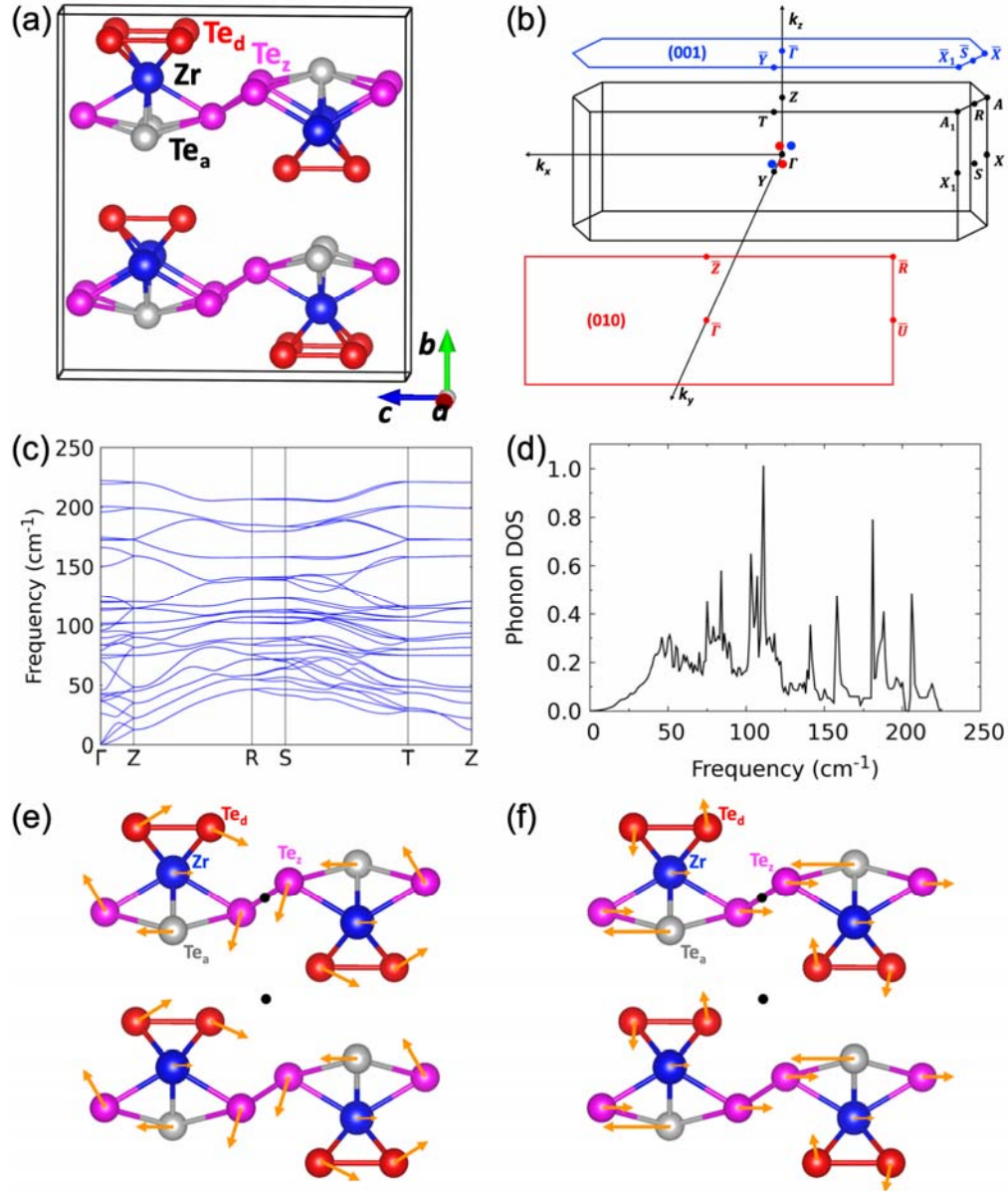


Figure 1. (a) Base-centered orthorhombic structure of ZrTe_5 in space group 63 ($Cmcm$) with different sites of Zr, apical Te (Te_a), dimer Te (Te_d) and zigzag Te (Te_z) labeled. (b) Bulk, (001) and (010) surface Brillouin zones labeled with high symmetry points. Large red and blue circles are the two pairs of Weyl points induced with B_{1u} lattice distortion. (c) Calculated phonon dispersion and (d) phonon density of states (DOS). (e) First and (f) second lowest B_{1u} infrared phonon mode with lattice distortion shown by arrows, respectively. Black circles show the broken inversion centers.

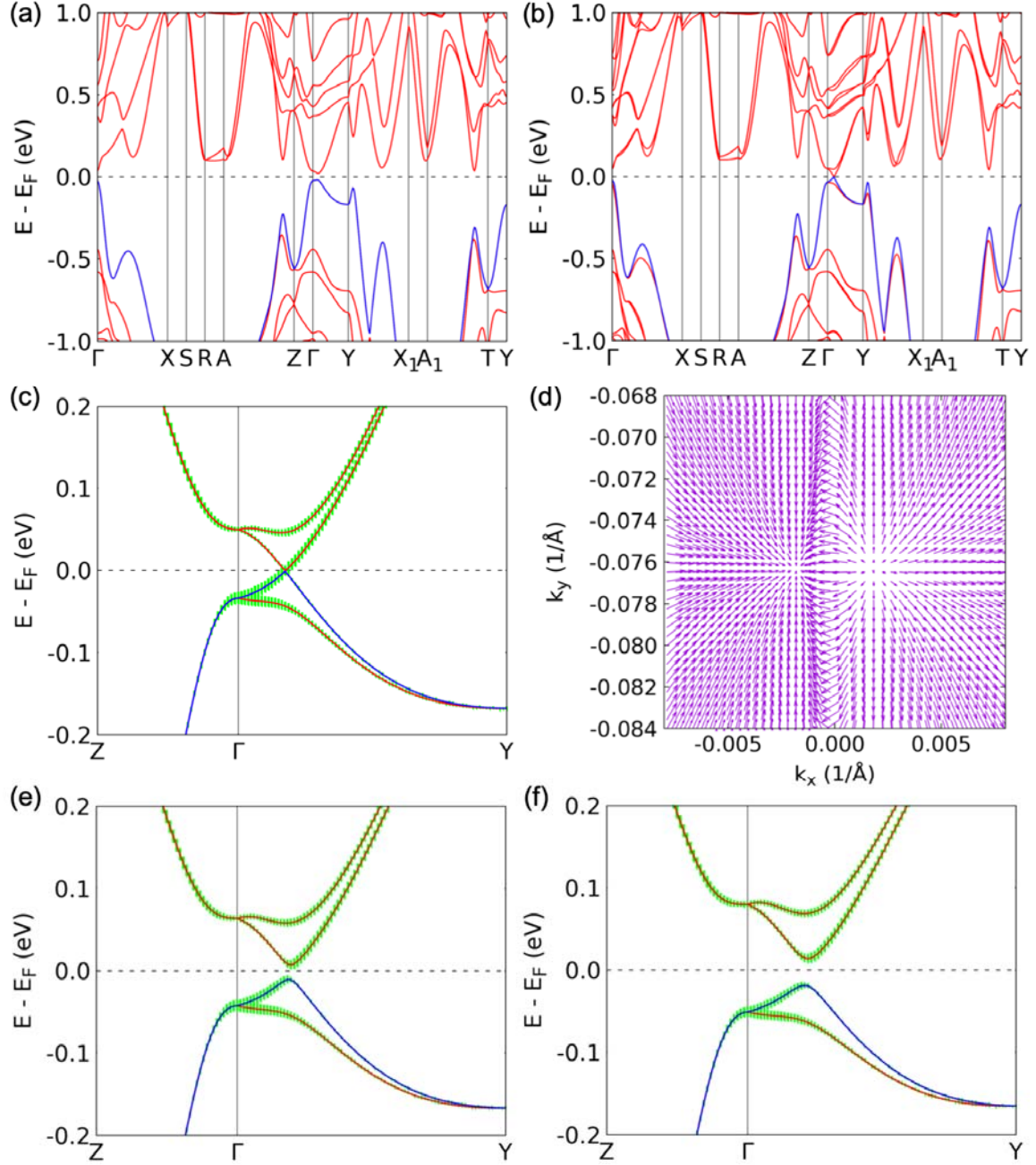


Figure 2. Band structures of ZrTe₅ in experimental lattice parameters without (a) and with (b) the second lowest B_{1u} (44.1 cm^{-1}) lattice distortion of magnitude $\lambda=1.0$. (c) Band structure of (b) zoomed in along Z- Γ -Y with projection (green shadow) on Te_d p orbitals. The top valence band is shown in blue. (d) Source and sink of Berry curvature on k_x - k_y plane at $k_z=0.0$ showing a pair of Weyl points near Γ as labeled in Fig.1(e). Panel (e) and (f) are the same as (c) with the increased magnitude of B_{1u} lattice distortion at $\lambda=1.5$ and $\lambda=2.0$.

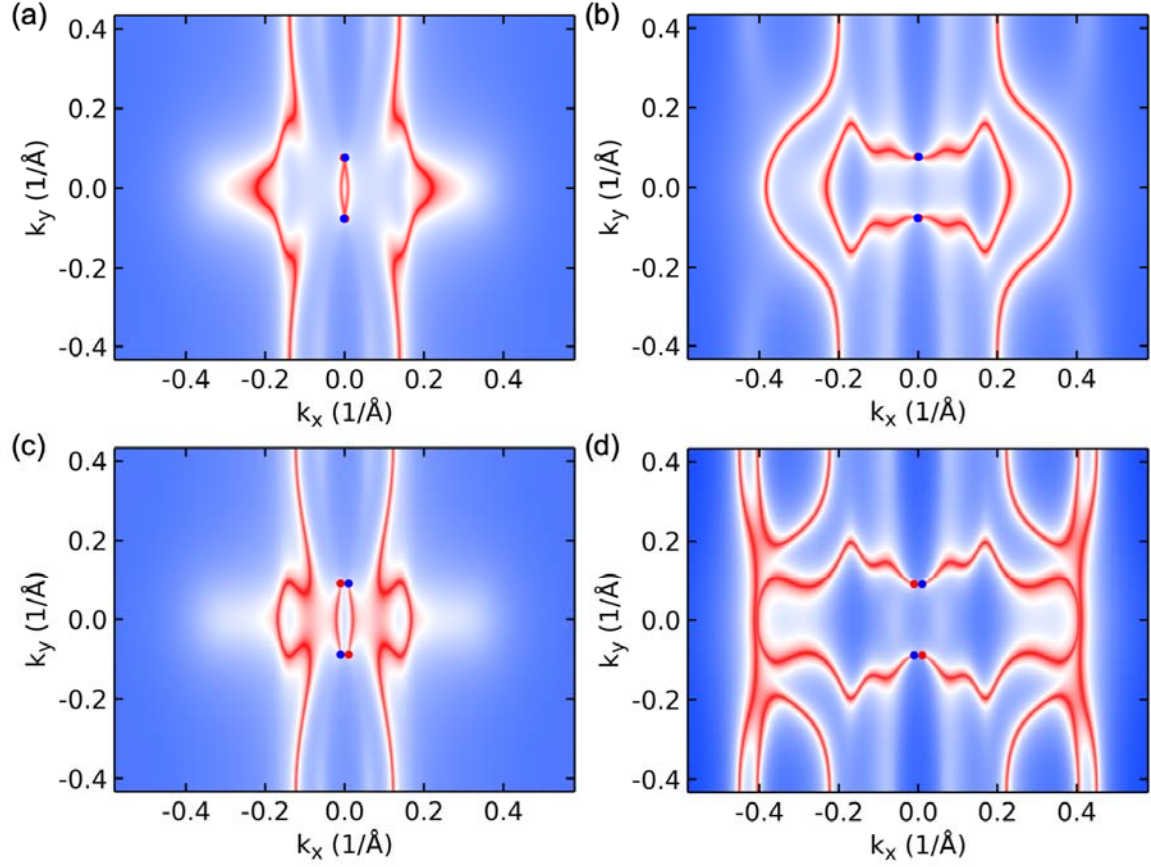


Figure 3. ZrTe₅ (001) surface 2D Fermi surface (FS) with the second lowest B_{1u} lattice distortion of different magnitude $\lambda=1.0$ ((a) and (b)) and $\lambda=1.5$ ((c) and (d)) at Weyl point binding energy. Panel (a) and (c) are the (001) top, and (b) and (d) are the (001) bottom surfaces. Low, medium, and high density of states is indicated by blue, white and red colors, respectively. Red (blue) circles label the Weyl point projection with Chern number $C=+1(-1)$.

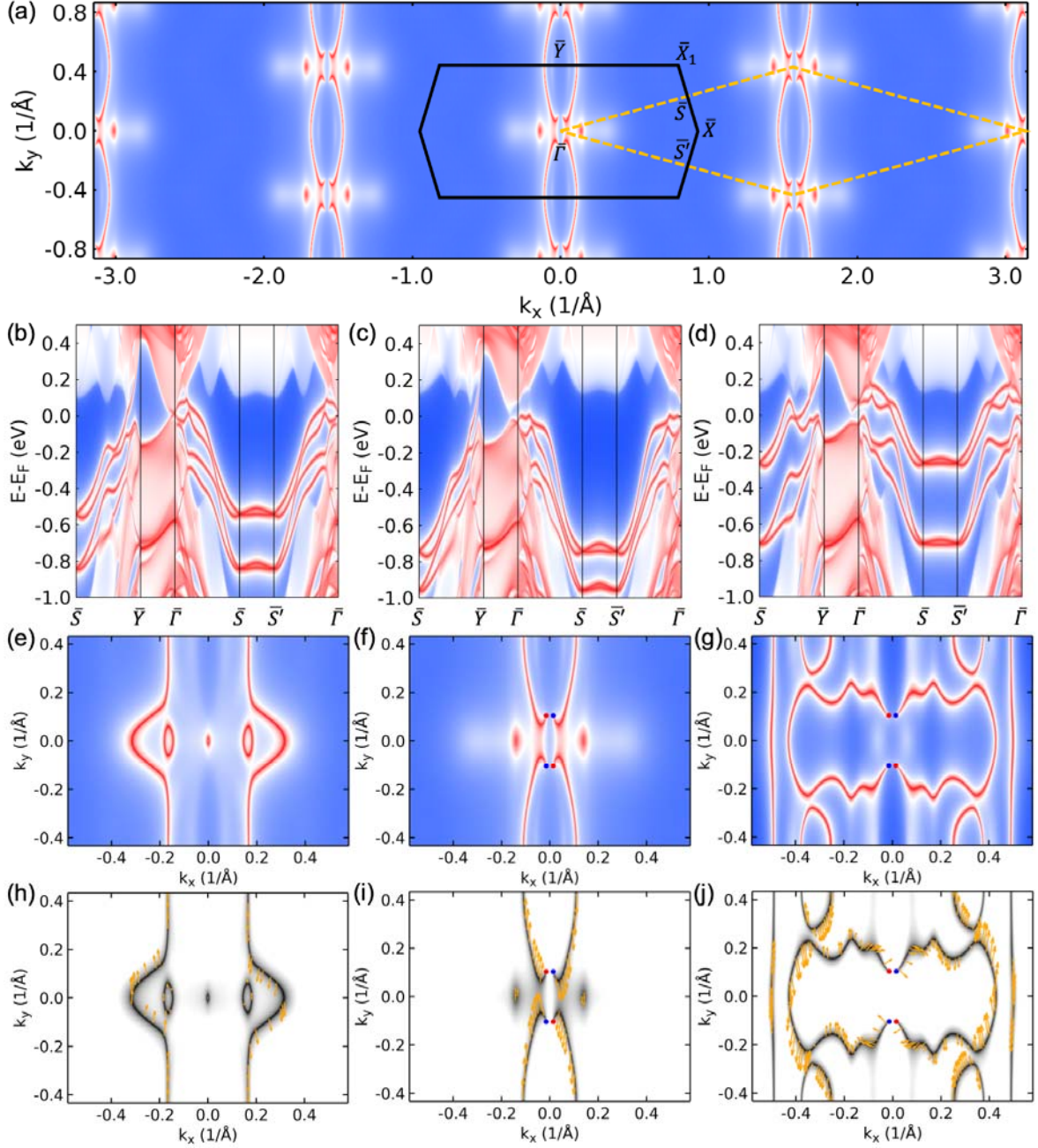


Figure 4. ZrTe₅ (001) surface states and 2D FS at E_F+9 meV. (a) 2D FS with the second lowest B_{lu} lattice distortion of magnitude $\lambda=2.0$ zoomed out to show the surface reciprocal unit cell (orange) and Brillouin zone (black) with high symmetry points labeled. Panel (b), (e) and (h) are the surface states, 2D FS and spin texture, respectively, on (001) surface of the STI without lattice distortion. Panel (c), (f) and (i) are those on the (001) top surface of the WSM with B_{lu} lattice distortion. Panel (d), (g) and (j) are those on the (001) bottom surface of the WSM with B_{lu} lattice distortion. Low, medium, and high density of states is indicated by blue, white and red colors, respectively. In (f), (g), (i) and (j), red (blue) circles label the Weyl point projection with Chern number $C=+1(-1)$.

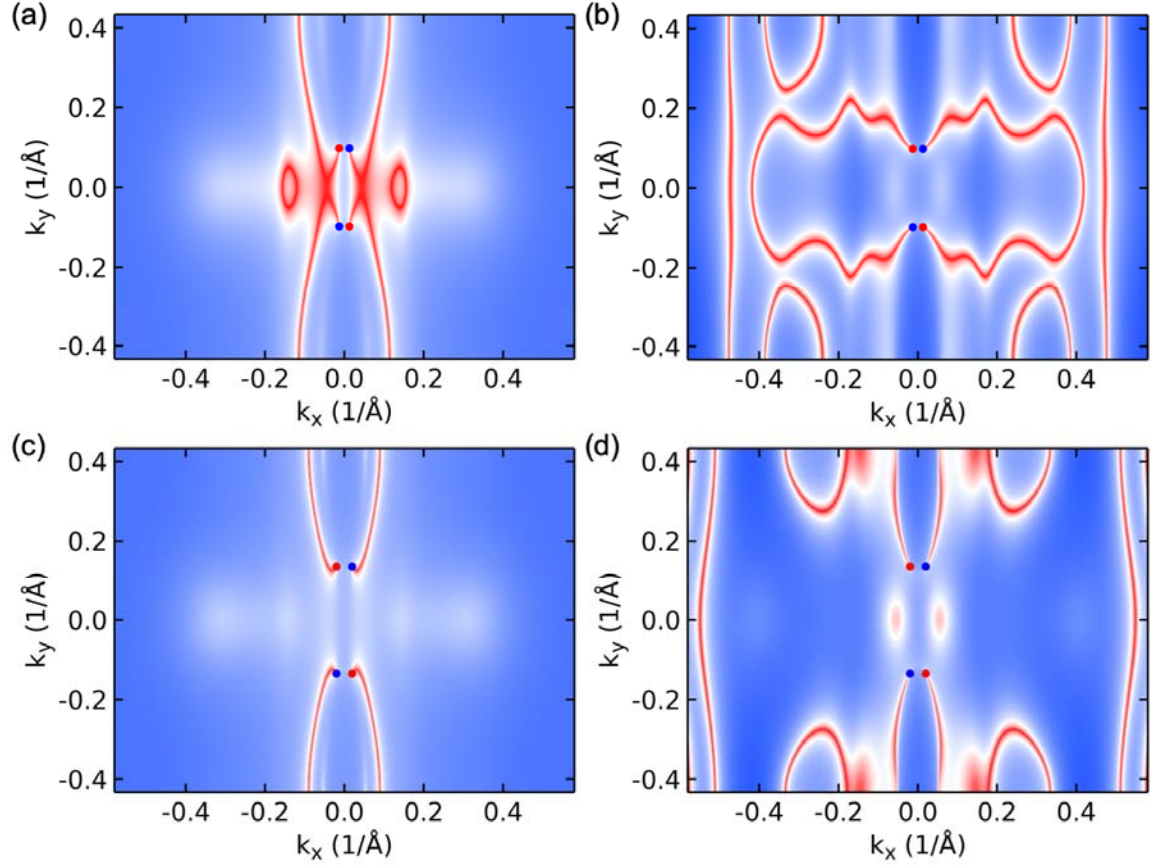


Figure 5. ZrTe₅ (001) surface 2D FS with the second lowest B_{1u} lattice distortion of different magnitude $\lambda=1.8$ ((a) and (b)) and $\lambda=3.0$ ((c) and (d)) at Weyl point binding energy. Panel (a) and (c) are the (001) top, and (b) and (d) are the (001) bottom surfaces. Low, medium, and high density of states is indicated by blue, white and red colors, respectively. Red (blue) circles label the Weyl point projection with Chern number $C=+1(-1)$.

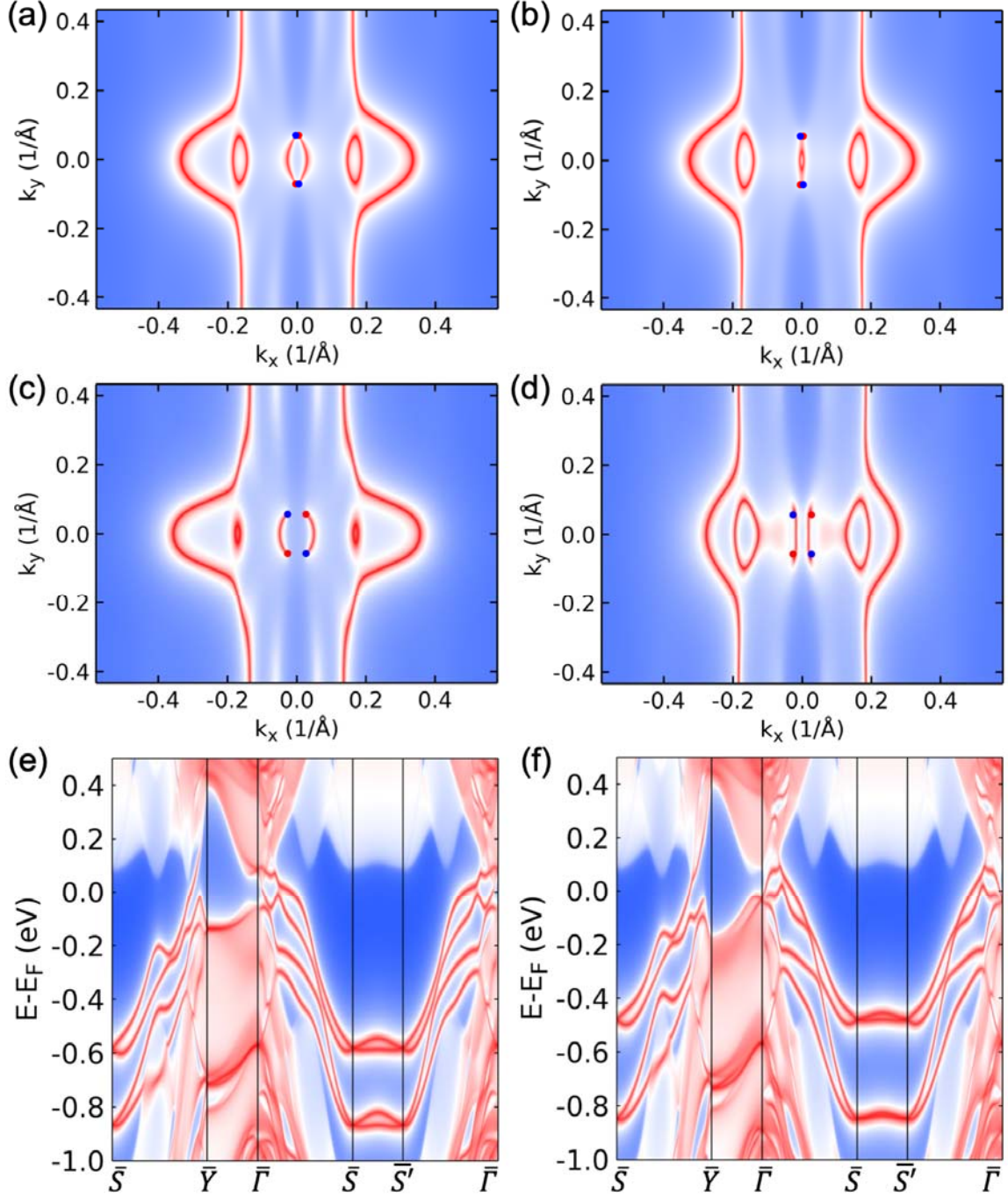


Figure 6. ZrTe₅ (001) surface 2D FS with the first lowest B_{1u} lattice distortion of different magnitude $\lambda=2.0$ ((a) and (b)) and $\lambda=6.0$ ((c) and (d)) at Weyl point binding energy. (e) and (f) The surface spectral functions for $\lambda=6.0$. Panel (a), (c) and (e) are the (001) top, and (b), (d) and (f) are the (001) bottom surfaces. Low, medium, and high density of states is indicated by blue, white and red colors, respectively. Red (blue) circles label the Weyl point projection with Chern number $C=+1(-1)$.

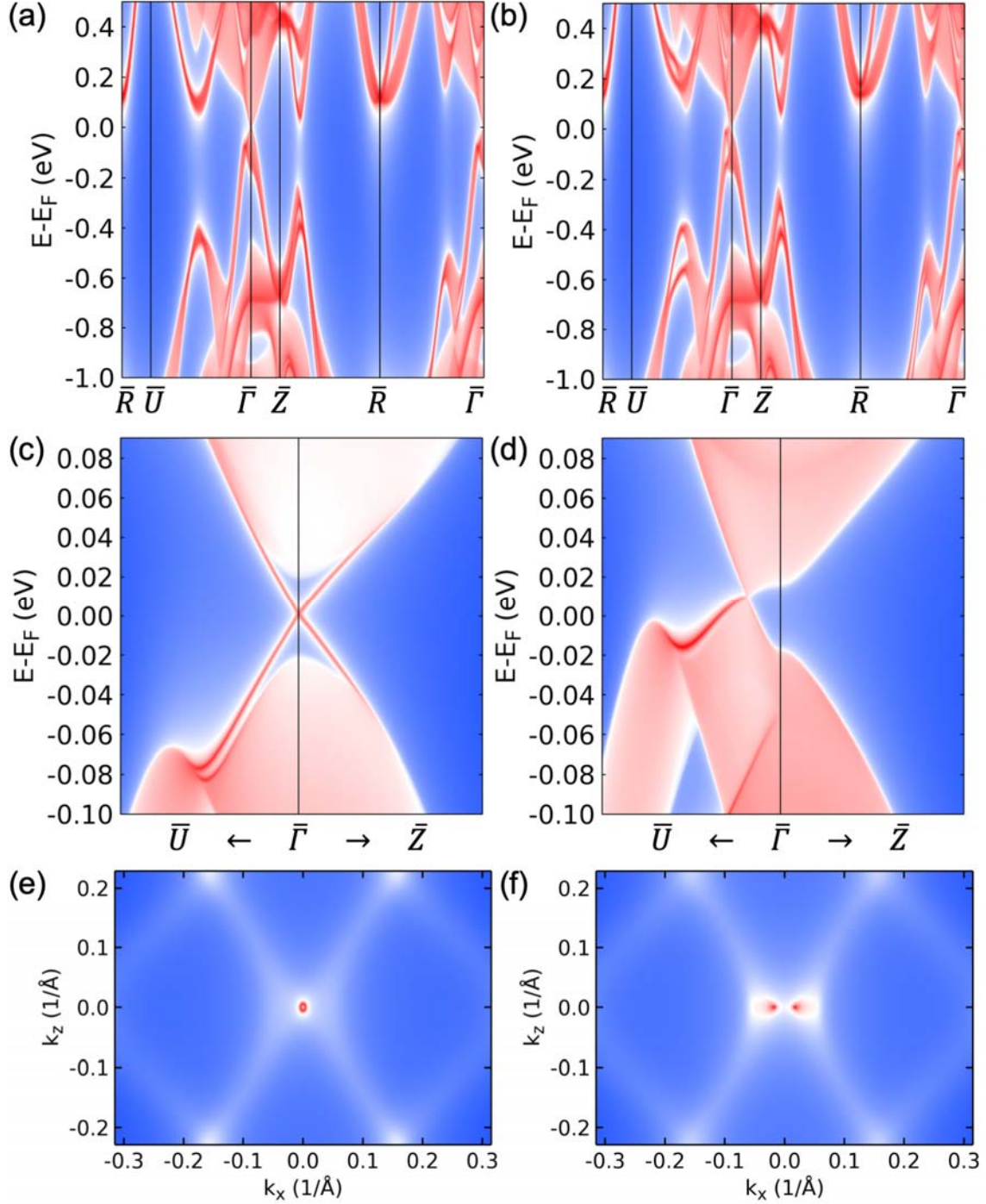


Figure 7. ZrTe₅ (010) surface states and 2D FS at E_F+9 meV. Panel (a), (c) and (e) are the surface states, zoom-in, 2D FS of the STI, respectively, without lattice distortion. Panel (b), (d) and (f) are those for WSM with the second lowest B_{lu} lattice distortion of magnitude $\lambda=2.0$. Low, medium, and high density of states is indicated by blue, white and red colors, respectively. In (f), a pair of Weyl points with opposite chirality are projected on top of each other.

References

1. N. P. Armitage, E. J. Mele, A. Vishwanath, Weyl and Dirac semimetals in three-dimensional solids. *Rev Mod Phys* **90**, 015001 (2018).
2. M. V. Berry, *Aspects of Degeneracy*. (Springer US, Boston, MA, 1985).
3. S. L. Adler, Axial-Vector Vertex in Spinor Electrodynamics. *Phys. Rev.* **177**, 2426-2438 (1969).
4. J. S. Bell, R. Jackiw, A Pcac Puzzle - π_0 -Gammagamma in Sigma-Model. *Nuovo Cimento A* **60**, 47 (1969).
5. H. B. Nielsen, M. Ninomiya, The Adler-Bell-Jackiw Anomaly and Weyl Fermions in a Crystal. *Phys Lett B* **130**, 389-396 (1983).
6. D. T. Son, B. Z. Spivak, Chiral anomaly and classical negative magnetoresistance of Weyl metals. *Phys Rev B* **88**, 104412 (2013).
7. A. A. Burkov, Chiral anomaly and transport in Weyl metals. *Journal of Physics: Condensed Matter* **27**, 113201 (2015).
8. K.-Y. Yang, Y.-M. Lu, Y. Ran, Quantum Hall effects in a Weyl semimetal: Possible application in pyrochlore iridates. *Phys Rev B* **84**, 075129 (2011).
9. C. K. Chan, P. A. Lee, K. S. Burch, J. H. Han, Y. Ran, When Chiral Photons Meet Chiral Fermions: Photoinduced Anomalous Hall Effects in Weyl Semimetals. *Phys Rev Lett* **116**, 026805 (2016).
10. Q. Ma, S. Y. Xu, C. K. Chan, C. L. Zhang, G. Q. Chang, Y. X. Lin, W. W. Xie, T. Palacios, H. Lin, S. Jia, P. A. Lee, P. Jarillo-Herrero, N. Gedik, Direct optical detection of Weyl fermion chirality in a topological semimetal. *Nat Phys* **13**, 842-+ (2017).
11. F. de Juan, A. G. Grushin, T. Morimoto, J. E. Moore, Quantized circular photogalvanic effect in Weyl semimetals. *Nat Commun* **8**, 15995 (2017).
12. D. Rees, K. Manna, B. Lu, T. Morimoto, H. Borrmann, C. Felser, J. E. Moore, D. H. Torchinsky, J. Orenstein, Observation of Topological Photocurrents in the Chiral Weyl Semimetal RhSi. *arXiv e-prints*. 2019.
13. A. C. Potter, I. Kimchi, A. Vishwanath, Quantum oscillations from surface Fermi arcs in Weyl and Dirac semimetals. *Nat Commun* **5**, 5161 (2014).
14. E. V. Gorbar, V. A. Miransky, I. A. Shovkovy, P. O. Sukhachov, Origin of dissipative Fermi arc transport in Weyl semimetals. *Phys Rev B* **93**, 235127 (2016).
15. Y. Zhang, D. Bulmash, P. Hosur, A. C. Potter, A. Vishwanath, Quantum oscillations from generic surface Fermi arcs and bulk chiral modes in Weyl semimetals. *Sci Rep-Uk* **6**, 23741 (2016).
16. S. A. Parameswaran, T. Grover, D. A. Abanin, D. A. Pesin, A. Vishwanath, Probing the Chiral Anomaly with Nonlocal Transport in Three-Dimensional Topological Semimetals. *Phys Rev X* **4**, 031035 (2014).

17. G. Q. Chang, S. Y. Xu, B. J. Wieder, D. S. Sanchez, S. M. Huang, I. Belopolski, T. R. Chang, S. T. Zhang, A. Bansil, H. Lin, M. Z. Hasan, Unconventional Chiral Fermions and Large Topological Fermi Arcs in RhSi. *Phys Rev Lett* **119**, 206401 (2017).
18. P. Tang, Q. Zhou, S.-C. Zhang, Multiple Types of Topological Fermions in Transition Metal Silicides. *Phys Rev Lett* **119**, 206402 (2017).
19. G. Chang, B. J. Wieder, F. Schindler, D. S. Sanchez, I. Belopolski, S.-M. Huang, B. Singh, D. Wu, T.-R. Chang, T. Neupert, S.-Y. Xu, H. Lin, M. Z. Hasan, Topological quantum properties of chiral crystals. *Nat Mater* **17**, 978-985 (2018).
20. D. S. Sanchez, I. Belopolski, T. A. Cochran, X. Xu, J.-X. Yin, G. Chang, W. Xie, K. Manna, V. Süß, C.-Y. Huang, N. Alidoust, D. Multer, S. S. Zhang, N. Shumiya, X. Wang, G.-Q. Wang, T.-R. Chang, C. Felser, S.-Y. Xu, S. Jia, H. Lin, M. Z. Hasan, Topological chiral crystals with helicoid-arc quantum states. *Nature* **567**, 500-505 (2019).
21. L. L. Wang, N. H. Jo, B. Kuthanazhi, Y. Wu, R. J. McQueeney, A. Kaminski, P. C. Canfield, Single pair of Weyl fermions in the half-metallic semimetal EuCd₂As₂. *Phys Rev B* **99**, 245147 (2019).
22. N. H. Jo, B. Kuthanazhi, Y. Wu, E. Timmons, T.-H. Kim, L. Zhou, L.-L. Wang, B. G. Ueland, A. Palasyuk, D. H. Ryan, R. J. McQueeney, K. Lee, B. Schruck, A. A. Burkov, R. Prozorov, S. L. Bud'ko, A. Kaminski, P. C. Canfield, Manipulating magnetism in the topological semimetal EuCd₂As₂. *Phys Rev B* **101**, 140402 (2020).
23. L. L. Wang, N. H. Jo, Y. Wu, Q. Wu, A. Kaminski, P. C. Canfield, D. D. Johnson, Phonon-induced topological transition to a type-II Weyl semimetal. *Phys Rev B* **95**, 165114 (2017).
24. J. C. Y. Teo, L. Fu, C. L. Kane, Surface states and topological invariants in three-dimensional topological insulators: Application to Bi_{1-x}Sb_x. *Phys Rev B* **78**, 045426 (2008).
25. N. Morali, R. Batabyal, P. K. Nag, E. Liu, Q. Xu, Y. Sun, B. Yan, C. Felser, N. Avraham, H. Beidenkopf, Fermi-arc diversity on surface terminations of the magnetic Weyl semimetal Co₃Sn₂S₂. *Science* **365**, 1286-1291 (2019).
26. H. M. Weng, X. Dai, Z. Fang, Transition-Metal Pentatelluride ZrTe₅ and HfTe₅: A Paradigm for Large-Gap Quantum Spin Hall Insulators. *Phys Rev X* **4**, 011002 (2014).
27. Q. Li, D. E. Kharzeev, C. Zhang, Y. Huang, I. Pletikosic, A. V. Fedorov, R. D. Zhong, J. A. Schneeloch, G. D. Gu, T. Valla, Chiral magnetic effect in ZrTe₅. *Nat Phys* **12**, 550-555 (2016).
28. G. Manzoni, L. Gragnaniello, G. Autes, T. Kuhn, A. Sterzi, F. Cilento, M. Zacchigna, V. Enenkel, I. Vobornik, L. Barba, F. Bisti, P. Bugnon, A. Magrez, V. N. Strocov, H. Berger, O. V. Yazyev, M. Fonin, F. Parmigiani, A. Crepaldi, Evidence for a Strong Topological Insulator Phase in ZrTe₅. *Phys Rev Lett* **117**, 237601 (2016).
29. T. Liang, J. J. Lin, Q. Gibson, S. Kushwaha, M. H. Liu, W. D. Wang, H. Y. Xiong, J. A. Sobota, M. Hashimoto, P. S. Kirchmann, Z. X. Shen, R. J. Cava, N. P. Ong, Anomalous Hall effect in ZrTe₅. *Nat Phys* **14**, 451-456 (2018).

30. P. Shahi, D. J. Singh, J. P. Sun, L. X. Zhao, G. F. Chen, Y. Y. Lv, J. Li, J. Q. Yan, D. G. Mandrus, J. G. Cheng, Bipolar Conduction as the Possible Origin of the Electronic Transition in Pentatellurides: Metallic vs Semiconducting Behavior. *Phys Rev X* **8**, 021055 (2018).
31. L. L. Wang, A. Kaminski, P. C. Canfield, D. D. Johnson, Different Topological Quantum States in Ternary Zintl compounds: BaCaX (X = Si, Ge, Sn and Pb). *Journal of Physical Chemistry C* **122**, 705-713 (2018).
32. B. Xu, L. X. Zhao, P. Marsik, E. Sheveleva, F. Lyzwa, Y. M. Dai, G. F. Chen, X. G. Qiu, C. Bernhard, Temperature-Driven Topological Phase Transition and Intermediate Dirac Semimetal Phase in ZrTe₅. *Phys Rev Lett* **121**, 187401 (2018).
33. Z. J. Fan, Q. F. Liang, Y. B. Chen, S. H. Yao, J. Zhou, Transition between strong and weak topological insulator in ZrTe₅ and HfTe₅. *Sci Rep-Uk* **7**, 45667 (2017).
34. J. Mutch, W. C. Chen, P. Went, T. M. Qian, I. Z. Wilson, A. Andreev, C. C. Chen, J. H. Chu, Evidence for a strain-tuned topological phase transition in ZrTe₅. *Science Advances* **5**, eaav9771 (2019).
35. C. Vaswani, L. L. Wang, D. H. Mudiyansele, Q. Li, P. M. Lozano, G. D. Gu, D. Cheng, B. Song, L. Luo, R. H. J. Kim, C. Huang, Z. Liu, M. Mootz, I. E. Perakis, Y. Yao, K. M. Ho, J. Wang, Light-Driven Raman Coherence as a Nonthermal Route to Ultrafast Topology Switching in a Dirac Semimetal. *Phys Rev X* **10**, 021013 (2020).
36. P. Hohenberg, W. Kohn, Inhomogeneous Electron Gas. *Phys. Rev.* **136**, B864-B871 (1964).
37. W. Kohn, L. J. Sham, Self-Consistent Equations Including Exchange and Correlation Effects. *Phys. Rev.* **140**, A1133-A1138 (1965).
38. S. Baroni, S. de Gironcoli, A. Dal Corso, P. Giannozzi, Phonons and related crystal properties from density-functional perturbation theory. *Rev Mod Phys* **73**, 515-562 (2001).
39. J. P. Perdew, K. Burke, M. Ernzerhof, Generalized gradient approximation made simple. *Phys Rev Lett* **77**, 3865-3868 (1996).
40. S. Grimme, Semiempirical GGA-type density functional constructed with a long-range dispersion correction. *J Comput Chem* **27**, 1787-1799 (2006).
41. P. Giannozzi, O. Andreussi, T. Brumme, O. Bunau, M. B. Nardelli, M. Calandra, R. Car, C. Cavazzoni, D. Ceresoli, M. Cococcioni, N. Colonna, I. Carnimeo, A. Dal Corso, S. de Gironcoli, P. Delugas, R. A. DiStasio, A. Ferretti, A. Floris, G. Fratesi, G. Fugallo, R. Gebauer, U. Gerstmann, F. Giustino, T. Gorni, J. Jia, M. Kawamura, H. Y. Ko, A. Kokalj, E. Kucukbenli, M. Lazzeri, M. Marsili, N. Marzari, F. Mauri, N. L. Nguyen, H. V. Nguyen, A. Otero-de-la-Roza, L. Paulatto, S. Ponce, D. Rocca, R. Sabatini, B. Santra, M. Schlipf, A. P. Seitsonen, A. Smogunov, I. Timrov, T. Thonhauser, P. Umari, N. Vast, X. Wu, S. Baroni, Advanced capabilities for materials modelling with QUANTUM ESPRESSO. *J Phys-Condens Mat* **29**, 465901 (2017).
42. H. J. Monkhorst, J. D. Pack, Special Points for Brillouin-Zone Integrations. *Phys Rev B* **13**, 5188-5192 (1976).

43. T. Matkovic, P. Matkovic, Constitutional Study of the Titanium, Zirconium and Hafnium Tellurides. *Metalurgija (Zagreb)* **31**, 107-110 (1992).
44. G. Kresse, J. Furthmuller, Efficient Iterative Schemes for Ab initio Total-Energy Calculations Using a Plane-Wave Basis Set. *Phys Rev B* **54**, 11169-11186 (1996).
45. G. Kresse, J. Furthmuller, Efficiency of Ab-initio Total Energy Calculations for Metals and Semiconductors Using a Plane-Wave Basis Set. *Comp Mater Sci* **6**, 15-50 (1996).
46. P. E. Blöchl, Projector Augmented-Wave Method. *Phys Rev B* **50**, 17953-17979 (1994).
47. A. Togo, I. Tanaka, First principles phonon calculations in materials science. *Scripta Materialia* **108**, 1-5 (2015).
48. N. Marzari, D. Vanderbilt, Maximally localized generalized Wannier functions for composite energy bands. *Phys Rev B* **56**, 12847-12865 (1997).
49. I. Souza, N. Marzari, D. Vanderbilt, Maximally localized Wannier functions for entangled energy bands. *Phys Rev B* **65**, 035109 (2001).
50. D. H. Lee, J. D. Joannopoulos, Simple Scheme for Surface-Band Calculations .1. *Phys Rev B* **23**, 4988-4996 (1981).
51. D. H. Lee, J. D. Joannopoulos, Simple Scheme for Surface-Band Calculations .2. The Greens-Function. *Phys Rev B* **23**, 4997-5004 (1981).
52. M. P. L. Sancho, J. M. L. Sancho, J. Rubio, Quick Iterative Scheme for the Calculation of Transfer-Matrices - Application to Mo(100). *J Phys F Met Phys* **14**, 1205-1215 (1984).
53. M. P. L. Sancho, J. M. L. Sancho, J. Rubio, Highly Convergent Schemes for the Calculation of Bulk and Surface Green-Functions. *J Phys F Met Phys* **15**, 851-858 (1985).
54. Q. Wu, S. Zhang, H.-F. Song, M. Troyer, A. A. Soluyanov, WannierTools: An open-source software package for novel topological materials. *Computer Physics Communications* **224**, 405-416 (2018).
55. J. P. Perdew, A. Ruzsinszky, G. I. Csonka, O. A. Vydrov, G. E. Scuseria, L. A. Constantin, X. Zhou, K. Burke, Restoring the Density-Gradient Expansion for Exchange in Solids and Surfaces. *Phys Rev Lett* **100**, 136406 (2008).
56. G. Landa, A. Zwick, R. Carles, M. A. Renucci, A. Kjekshus, Lattice-Dynamics of the Transition-Metal Pentatellurides ZrTe₅ and HfTe₅. *Solid State Commun* **50**, 297-302 (1984).
57. D. M. Ceperley, B. J. Alder, Ground-State of the Electron-Gas by a Stochastic Method. *Phys Rev Lett* **45**, 566-569 (1980).
58. J. P. Perdew, A. Zunger, Self-Interaction Correction to Density-Functional Approximations for Many-Electron Systems. *Phys Rev B* **23**, 5048-5079 (1981).
59. L. Fu, C. L. Kane, Topological insulators with inversion symmetry. *Phys Rev B* **76**, 045302 (2007).